City, University of London Institutional Repository

Modelling flow-induced microstructural segregation in semi-solid metals

Zhen Ma [a,b], Huarui Zhang [a,1], Hanwei Fu [a], Joana Fonseca [b], Yanzhao Yang [a], Ming Du [c], Hu Zhang [a,c,*]

[a] School of Materials Science and Engineering, Beihang University, Beijing 100191, China
[b] Department of Civil Engineering, City, University of London, London EC1V 0HB, UK
[c] Ningbo Institute of Technology, Beihang University, Ningbo 315832, China

HIGHLIGHTS

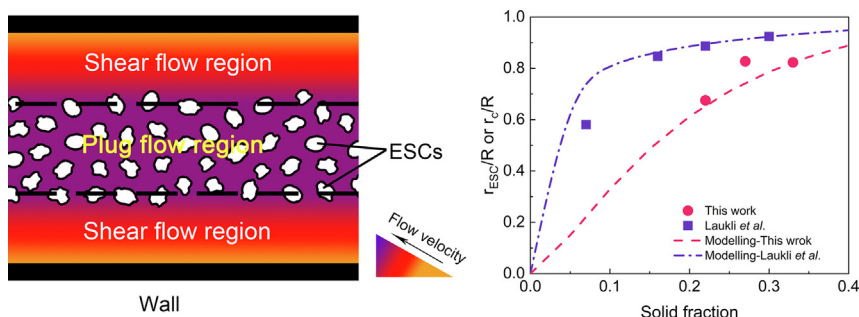- Externally solidified crystals (ESCs) migration model is proposed for flow-induced microstructural segregation.
- Real-time in situ X-ray synchrotron radiography of semi-solid metal flow is conducted.
- In-situ and validation experimental results support the ESCs migration model.
- The segregation is controllable by adjusting process parameters.

GRAPHICAL ABSTRACT

ARTICLE INFO

ABSTRACT

Lightweight alloys produced by pressurized castings suffer from flow-induced microstructural segregation due to the migration of externally solidified crystals (ESCs). Although some qualitative research has been carried out on ESCs migration, quantitative prediction of it is still demanded. In this respect, an ESCs migration model based on hydrodynamics and the rheological behaviour of semi-solid metals (SSMs) is proposed to estimate flow-induced microstructural segregation. By employing the model, a plug flow region having a decisive influence on ESCs migration is observed according to the flow simulation of yield-pseudoplastic SSMs. Good agreement between the experimental data and the simulation results is obtained, suggesting that such flow-induced microstructural segregation is controllable by manipulating process parameters such as solid fraction, cavity size and filling velocity. A real-time in situ synchrotron X-ray radiography experiment is carried out to reveal the nature of ESCs migration and provide evidence for the hypothesized flow-induced ESCs migration mechanism. A semi-empirical solid fraction-related rheological (SFR) model capable of relating rheological parameters with solid fraction of SSMs is also proposed, enabling the optimization of process parameters.

1. Introduction

Lightweight alloys such as aluminium alloys and magnesium alloys are widely used in automotive industry and electronic industry owing to their high specific strength [1,2]. Pressurized castings such as high pressure die casting (HPDC) and squeeze casting are common methods to produce thin-wall and complex-shaped lightweight alloys [3–5]. The main characteristic of pres-

* Corresponding author at: School of Materials Science and Engineering, Beihang University, Beijing 100191, China.
E-mail addresses: huarui@buaa.edu.cn (H. Zhang), zhanghu@buaa.edu.cn (H. Zhang).
[1] Principal corresponding author.

surized castings is the applied pressure introduced to help the filling and feeding processes in order to avoid misrun and shrinkage porosity. However, components produced by pressurized castings suffer from defects such as surface blistering, microstructural segregation and porosity [6–9].

The segregation of externally solidified crystals (ESCs) is relatively common in HPDC lightweight alloys [10,11]. ESCs arise from two sources: (i) crystals solidified due to temperature decrease when the melt is held in a cold chamber before the filling process; (ii) solid particles in the semi-solid slurry during HPDC [12]. These ESCs diffusing in semi-solid metals (SSMs) move with the solid–liquid mixture in the subsequent filling process. Normally ESCs are found to exhibit an inhomogeneous distribution throughout the microstructural of solidified components. ESCs tend to concentrate at the central part of a casting, causing microstructural segregation and hence, leading to the deterioration of mechanical properties [12]. Both the size and spatial distribution of ESCs are believed to have significant influence on the strength and plasticity of castings [7,13,14]. In this respect, understanding the segregation behaviour of ESCs is crucial for process optimization to eliminate the microstructural segregation.

A number of mechanisms have been proposed by Laukli et al. [12] to describe ESCs segregation. Among them, the flow-related lift mechanism is most widely accepted [15,16]. According to the flow-related lift mechanism, ESCs segregation is strongly related to the flow of SSMs during filling process. The non-linear velocity profile i.e. the changing shear rate of SSMs flowing across the radial direction is thought to be the key influence factor for ESCs segregation. For SSMs which behave like non-Newtonian fluid, the shear rate is not constant when the SSMs flow along the runner and mould, i.e., the flow velocity increases and the shear rate decreases along the radial direction towards the central part. Thus, it can be inferred that the solid particles are forced to migrate from the wall to the centre due to the higher velocity difference between the particle and the liquid near the wall. Additionally, the Magnus lift force caused by the spinning of the particles can also induce the movement of the particles toward the region of higher velocity. It can thus be expected that both the non-linear velocity profile and the Magnus lift force could contribute to the migration of ESCs.

However, most of previously published studies focused on the influence of casting parameters, such as the solid fraction (pouring temperature) of SSM, die temperature and filling velocity on ESCs segregation, and qualitatively explained the experimental results with the flow-related lift mechanism [10,12,14–17]. The absence of a quantitative model limits further research and theory application to reduce and potentially avoid ESCs segregation, thus, improving casting quality. It is clear that the flow-related migration hypothesis is dependent on the flow behaviour of SSMs. Hence, analysing and modelling the flow behaviour of SSMs is believed to provide a new solution to the quantification of ESCs segregation.

The flow behaviour of SSMs is determined by the rheological behaviour of SSMs and casting parameters [18–20]. Thus far, studies have suggested that SSMs are pseudoplastic (shear thinning) with the most significant feature being the viscosity decrease with the increase in shear rate [21–27]. A number of rheological models, which are fundamental for the current numerical modelling of SSM flow, have been proposed under this premise [21,24,28]. More recently, further research lead to redefining SSMs as yield-pseudoplastic fluid thanks to the observation of yield stress in SSMs [29]. In this respect, yield stress can be defined as the critical point of shear stress at which the SSMs begin to flow. In other words, the yield stress implies that SSMs behave like "solid" when the applied shear stress is below the yield stress, while SSM flow as "liquid" if the yield stress is exceeded. Based on this, Herschel-

Bulkley (HB) model [30] is introduced to describe the rheological behaviour of SSMs:

$$\tau(\dot{\gamma}) = \tau_y + K\dot{\gamma}^n \qquad (1)$$

where τ is the shear stress, τ_y is the yield stress, K is the consistency factor, $\dot{\gamma}$ is the shear rate and n is the flow exponent. The yield stress, consistency factor and flow exponent are rheological parameters which are determined by the natural properties of the fluid. The shear stress and shear rate are variables which represent the applied shear force per unit area and the velocity gradient in a flowing fluid, respectively. The flow exponent value $n = 1$, $n < 1$ and $n > 1$ corresponds to Bingham fluid, yield-pseudoplastic fluid and yield dilatant fluid, respectively [31]. The applicability of HB model for SSMs has been verified by its reasonable flow exponent and consistency with the experimental data in our previously study [32].

The rheological parameters are found to be significantly affected by temperature which determines the solid fraction of SSMs on account of the quantity and morphology of the solid particles dispersed in the liquid phase [21]. Establishing the relationship between the rheological parameters and the solid fraction is a widely used method to improve rheological models [26,33,34]. Conventionally, the relationship is modelled by fitting the rheological parameters with respect to solid fraction by linear or exponential equations. However, this approach causes a major drawback: they are only applicable in a narrow solid fraction range without the boundary conditions (reasonable rheological parameters at the solid fraction of 0 and 1) being satisfied. This issue may limit the generalization and application of the approach. Therefore, a model which not only is consistent with the experimental data, with the boundary conditions satisfied, but also meets the underlying mechanism of the rheological behaviour of SSMs, should be established for SSMs flow.

To quantitatively model the microstructural segregation caused by the migration of ESCs, an ESCs migration model based on the flow modelling of SSMs is proposed in this study. The key factor responsible for ESCs migration is analysed, where a semi-empirical solid fraction-related rheological (SFR) model for describing SSMs flow is established by relating the rheological parameters of HB model with solid fraction with boundary conditions satisfied. The prediction of the ESCs segregation area sizes yielded by the proposed model is compared with the experimental observations for validation.

2. ESCs migration model

2.1. Yield stress and plug flow

As discussed previously, SSMs are a yield-pseudoplastic fluid instead of a pseudoplastic fluid. The crucial difference between these two types of fluid is that a yield stress, which works as the threshold value to determine whether the fluid flows or not, exist in a yield-pseudoplastic fluid but not in a pseudoplastic fluid. Different from a pseudoplastic fluid, there is a plug flow region in a yield-pseudoplastic fluid as a result of the yield stress during flow. For further studying the plug flow region, a typical fluid condition existing during the casting process, the Poiseuille flow [35] (steady state flow in a circular tube) of yield-pseudoplastic fluid is analysed hereafter. Considering a unit Poiseuille flow with the length of dL and according to conservation of momentum (the driving force equal to the shear stress), the shear stress τ at radius r is [35]:

$$\tau = \frac{r}{2}\frac{dp}{dL} \qquad (2)$$

where dp is the driving force of the unit, dp/dL is the pressure gradient accordingly. The shear stress reaches the maximum at $r = R$,

where R is the radius of the tube; and it decreases with decreasing radius, reaching the minimum value of 0 corresponding to $r = 0$. For a yield-pseudoplastic fluid, when the shear stress decreases to the yield stress with the corresponding radius being r_c, there is no relative motion (shear rate) between the flow layers in the region $r < r_c$ (plug flow region) where the SSMs act as solid, and the fluid in the plug flow region moves forward integrally with zero shear rate along the radial direction. While for the pseudoplastic fluid, relative motion exists across the entire radius with the absence of plug flow region. The comparison between the flow behaviours of yield-pseudoplastic fluid and pseudoplastic fluid is illustrated in Fig. 1. Both of the two fluids show non-linear velocity profile in the shear flow region: the shear rate decreasing with decreasing radius in the shear flow region.

2.2. Flow-induced ESCs migration

Since the non-linear velocity profile during SSMs flow is thought to be the origin of ESCs lift, it is reasonable to propose a flow-induced ESCs migration mechanism taking the plug flow region into consideration. For yield-pseudoplastic SSMs, ESCs lift only occurs in the shear flow region where non-linear velocity profile exists. During SSMs flow, the ESCs gradually move from the wall to the boundary between shear flow region and plug flow region due to the non-linear velocity profile in the shear flow region. After arriving the boundary, the ESCs will keep moving into the plug flow region because of the inertia effect. Subsequently, the ESCs will be intercepted by the plug flow region after the kinetic energy dissipates because there is no shear rate in the integrally moving plug flow region. In short, the flow-induced ESCs migration mechanism proposed is that the ESCs tend to be localized in the plug flow region of SSMs flow as a result of the absence of shearing.

Based on the above hypothesis, the flow behaviour of SSMs in the Poiseuille flow is modelled hereafter to describe the migration of ESCs in the filling process. Regarding SSMs as yield-pseudoplastic fluid, previously mentioned HB model (Eq. (1)) is employed as its rheological model for the SSMs flow.

The flow velocity ($u(r)$) of SSMs at the radius of r is:

$$u(r) = -\int_r^R \dot{\gamma}\mathrm{d}r \tag{3}$$

Substituting Eqs. (1) and (2) into Eq. (3), the velocity profile along the radial direction ($u_{HB}(r)$) and the average flow velocity ($\bar{u}_{HB}$) of yield-pseudoplastic SSMs are:

$$u_{HB}(r) = \begin{cases} \frac{n}{n+1}\left(\frac{1}{2K}\frac{\mathrm{d}p}{\mathrm{d}L}\right)^{\frac{1}{n}}\left[(R-r_c)^{\frac{n+1}{n}} - (r-r_c)^{\frac{n+1}{n}}\right] & r > r_c \\ \frac{n}{n+1}\left(\frac{1}{2K}\frac{\mathrm{d}p}{\mathrm{d}L}\right)^{\frac{1}{n}}(R-r_c)^{\frac{n+1}{n}} & r \leqslant r_c \end{cases} \tag{4}$$

and

$$\bar{u}_{HB} = \frac{\pi r_c^2 u(r_c) + \int_{r_c}^R 2\pi r u(r)\mathrm{d}r}{\pi R^2} \tag{5}$$

respectively, and r_c yields

$$r_c = 2\tau_y \frac{\mathrm{d}L}{\mathrm{d}p} \tag{6}$$

derived by substituting the yield stress τ_y into Eq. (2). It can be seen from Eq. (6) that the dimension of the plug flow region is determined by the yield stress and the pressure gradient along the axial direction. The pressure gradient can be calculated through Eqs. (4) and (5) with a given flow velocity of SSMs. Thus, the dimension of plug flow region i.e. ESCs migration area can finally be derived by solving Eqs. (4)–(6).
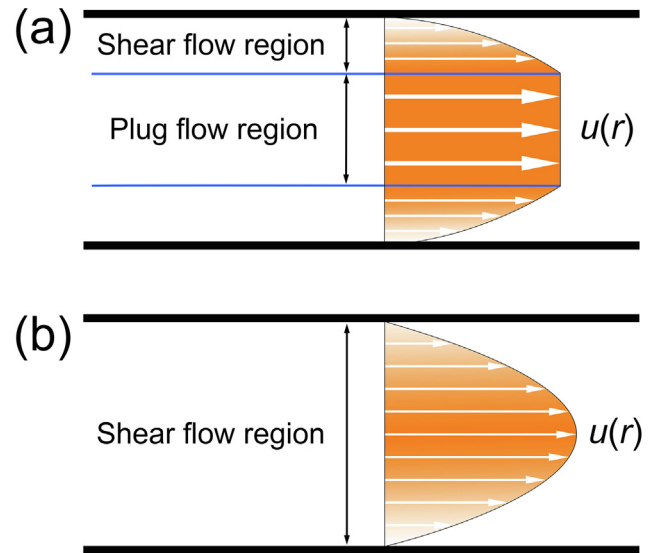

Fig. 1. Comparison between the flow behaviours of (a) a yield-pseudoplastic fluid and (b) a pseudoplastic fluid.

2.3. SFR model

The rheological parameters are essential for solving the above equations. In this study, a semi-solid A356 alloy is studied as an example in order to clarify the rheological parameters of SSMs. The yield stresses, flow exponents and consistency factor obtained by means of a rheological test and HB model fitting are illustrated in Fig. 2(a). The detailed rheological test method and data analysis can be found in Appendix A.

The yield stress, flow exponent and consistency of the HB model vary consistently with the solid fraction as shown in Fig. 2(a). These parameters are determined by the content, size, shape and the strength of the solid phase as well as the content and viscosity of the liquid phase. Note that the solid fraction, instead of the temperature, is used here as a variable, as the former is more relevant to the state of the material. The yield stress and consistency factor, both increase with increasing solid fraction; while the flow exponent shows an opposite trend. It can be expected that with increasing solid fraction, the content, shape complexity and volume of the dendrites increase, enhancing the network caused by inter-atomic interactions and coherent dendrites and thus raising the yield stress. Similarly, the consistency factor, which represents the basic viscosity of SSMs, is also affected by these parameters which slow down the flow after the network and coherent dendrites collapse by shearing. The decrease of the flow exponent with increasing solid fraction may be due to the increasing disagglomeration density (the number of disaggregate solid particle clusters per unit volume) of the solid particles. More solid particle clusters tend to form in higher solid fraction, leading to the increase of disagglomeration density with increasing shear rate, which aggravates the shear thinning phenomenon of SSMs and causes the decrease of flow exponent.

It is clear that the HB model needs modifications in order to be applied in the ESCs migration model due to the changing rheological parameters with solid fraction. In this respect, a semi-empirical SFR model is proposed by establishing mathematical relationships between the rheological parameters of HB model and the solid fraction of SSMs. The SFR model consists of three equations describing the yield stress τ_y, consistency factor K and flow exponent n, respectively.
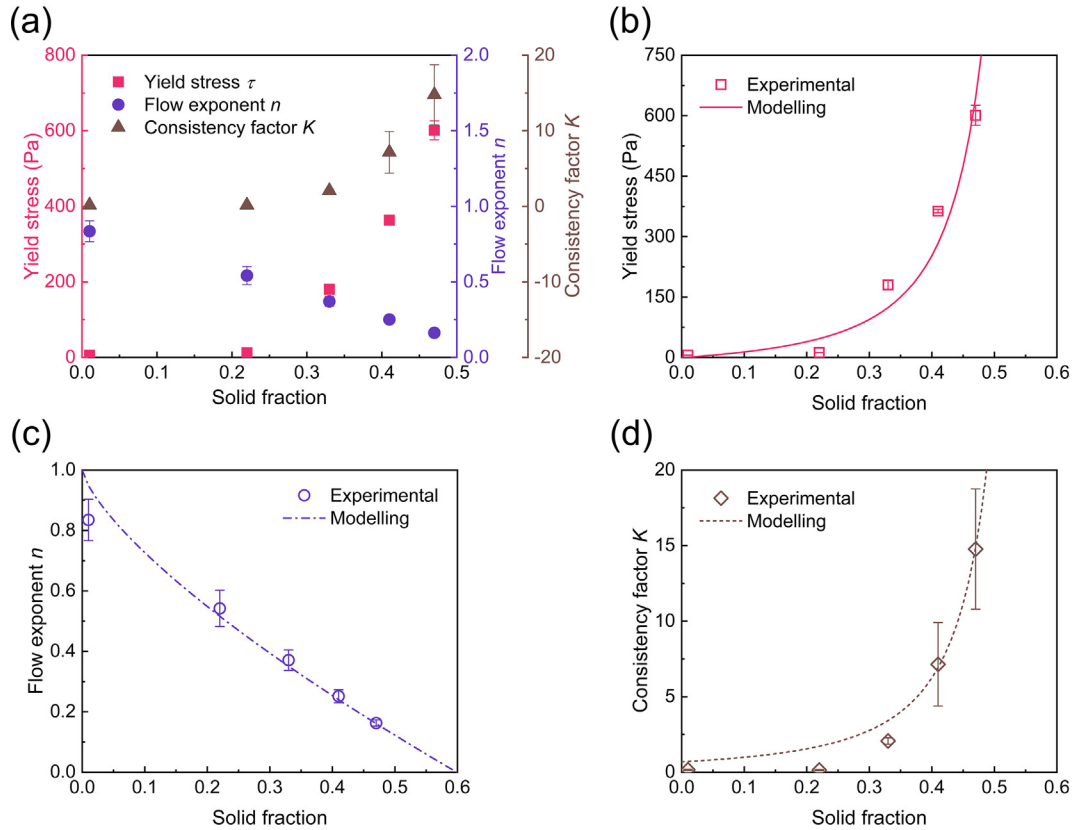
Fig. 2. (a) Yield stress, flow exponent and consistency factor of HB model versus solid fraction and comparison between experimental and the modelling results of (b) yield stress, (c) flow exponent and (d) consistency factor.

2.3.1. Consistency factor

Referring to Maron-Pierce viscosity model for the suspensions of spherical particles [36], the consistency factor of SSMs is represented in Eq. (7) if the morphology of the solid phase is regarded to be spherical:

$$\frac{K}{\eta_0} = \left(1 - \frac{f_s}{\phi_m}\right)^{-2} \tag{7}$$

where η_0 is the viscosity of liquid phase of SSMs; ϕ_m is the densest possible packing volume fraction for solid particles in SSMs. When $f_s \geqslant \phi_m$, the viscosity is infinite because SSMs are unable to flow due to the stacking of the solid particles within it.

The viscosity of liquid phase η_0 is estimated by the viscosity of the metal just above the liquidus temperature to be 0.590 Pa·s for A356 alloy (note that this value is measured by the same system as the rheology test of semi-solid A356 alloy to ensure the consistency of the data). The densest possible packing volume fraction ϕ_m is certainly lower than 1 for SSMs and it is believed to be equal to the solid fraction at which the solid particles of SSMs are coherent with each other. To calculate ϕ_m, a model for particles of arbitrary shape is introduced [37]: $\phi_m = 2/(0.32r_p + 3.02)$, where r_p is the average aspect ratio of the particles. The calculated ϕ_m is equal to 0.599 for spherical solid particles with $r_p = 1$.

2.3.2. Flow exponent

An empirical relationship for the flow exponent as a function of the solid fraction and the average aspect ratio is modified by substituting the particle volume fraction by the solid fraction of the model proposed for the suspensions of solid particles [37]: $n = 1 - ar_p(f_s/\phi_m)^b$, where $r_p = 1$ and $\phi_m = 0.599$ as previously stated; a and b are fitting parameters in the original equation.

Moreover, it is clear that when $f_s = \phi_m$, which means the solid fraction is the densest possible packing value and the SSMs behave extreme shear thinning property, n should equal to 0. That means ar_p should be equal to 1, leading to $a = 1$ for SSMs with $r_p = 1$. As a result, the flow exponent of SSMs with respect to solid fraction is:

$$n = 1 - \left(\frac{f_s}{\phi_m}\right)^b \tag{8}$$

By fitting the flow exponents of semi-solid A356 alloy, $b = 0.725$ with $R^2 = 0.950$.

2.3.3. Yield stress

For the yield stress, Heymann et al. [38] proposed a modified form of Maron-Pierce model, referring to which the yield stress of SSMs with respect to solid fraction can be calculated by:

$$\tau_y = \tau_0 \left(\left(1 - \frac{f_s}{\phi_m}\right)^{-2} - 1 \right) \tag{9}$$

where τ_0 is a fitting parameter. τ_0 is actually the yield stress at $f_s = \phi_m(1 - \sqrt{2}/2)$ ($f_s = 0.175$ for semi-solid A356 alloy) and is related to the size of the solid particles. The reasonable fitting results ($R^2 = 0.951$) of the yield stress of semi-solid A356 alloy gives $\tau_0 = 31.3$ Pa.

In short, the SFR model is established by the combination of Eqs. (7)–(9).

In contrast to other rheological parameter models of SSMs [26,39], either based on temperature or solid fraction, the SFR model has a major advantage on the satisfaction of boundary conditions. As shown in Table 1, the boundary conditions are the yield stress of 0 Pa and infinite, the flow exponent of 1 and 0, the consis-

Table 1
Boundary values of the rheological parameters of the SFR model.

Solid fraction f_s	Yield stress τ_y (Pa)	Flow exponent n	Consistency factor K
0	0	1 [40]	0.590
0.599 (ϕ_m)	∞	0	∞

tency factor of 0.590 and infinite at $f_s = 0$ and $f_s = \phi_m$, respectively. For the yield stress, its value is infinite as it is expected to be a rigid object at $f_s = \phi_m$; and it equals 0 Pa at $f_s = 0$, corresponding to the non-existence of yield stress at the liquid state. For the flow exponent, the value is equal to 1 at $f_s = 0$, which means that SSMs are Newtonian fluids at $f_s = 0$; and the value approaches 0 which demonstrates the extreme shear thinning property of SSMs as f_s approaches ϕ_m. For the consistency factor describing the basic viscosity of SSMs, it equals to 0.590 in line with the liquid viscosity at $f_s = 0$; and it approaches infinite at $f_s = \phi_m$, exhibiting the property of a solid body. Subsequently, the SFR model is used to model the three rheological parameters in the HB model. According to the comparison of experimental and modelling results shown in Fig. 2 (b), (c) and (d), the rheological parameters are well modelled by the SFR model. In summary, it has been shown in this section that the SFR model is capable of describing the rheological parameters including the yield stress, flow exponent and consistency factor in the HB model for the semi-solid A356 alloy. Furthermore, the SFR model provides a general way to model the rheological parameters of SSMs accounting for the boundary conditions.

Finally, the flow-induced microstructural segregation can be simulated by solving Eqs. (4)–(6) from the ESCs migration model using the rheological parameters calculated with the SFR model (the combination of Eqs. (7)–(9)). Accordingly, the ESCs migration area is determined by coupling the filling velocity and rheological parameters as a function of the solid fraction.

3. Experimental validation

3.1. Die filling experiment and results

In order to investigate the degrees of ESCs segregation under various solid fractions and filling velocities, a die filling experiment illustrated in Fig. 3 was carried out. A356 alloy ingots with the composition shown in Table A.1 were heated in a graphite crucible located in a resistance furnace and isothermally treated at 700 °C for 3 h to insure the melt of the alloy. Subsequently, the temperature of the furnace was set to three different temperatures (600 °C, 595 °C and 590 °C, respectively) corresponding to specific solid fractions (0.22, 0.27 and 0.33, respectively) of semi-solid A356 alloy. During the cooling process, the melt was stirred by a graphite rod coated with inorganic salt to obtain semi-solid slurry. The rotation rate of the rod was set to be 300 rpm (rpm) to fragment the dendrites of the ESCs. A type K thermocouple was placed at half depth of the melt to monitor the temperature.

When the desired temperature was reached, the graphite crucible was taken out of the furnace and the semi-solid slurry was poured into an H13 steel die. The die with the geometry as shown in Fig. 4(a) was preheated to ∼300 °C and coated by foundry coating. The open outlet of the die allowed the semi-solid slurry to flow continuously in the circular runner until solidification. The filling velocity, corresponding to the average flow velocity in Section 2, was controlled by adjusting the pouring height. Three pouring heights including 0 m, 0.5 m and 1 m higher than the inlet were applied; the corresponding filling velocities were v_1, v_2 and v_3, respectively.

Slice samples were cut from the radial cross section of the castings, located at 20 mm from the outlet, as shown in Fig. 4(a). Subsequently, the samples were grounded, polished and etched with 30% HCl, 10% HNO$_3$, 2% HF and 58% distilled water for 60 s to reveal the ESCs. Optical stereomicroscope was used to obtain the micrographs of the samples.

The experimental ESCs distributions of semi-solid A356 alloy at different filling velocities and solid fractions are shown as Fig. 4(b – f). It can be seen that the dimension of ESCs segregation area varies with the solid fraction and filling velocity. The dimension of the localized ESCs increases with increasing solid fraction and decreasing filling velocity.

3.2. Modelling results

The plug flow caused by the yield-pseudoplastic nature of SSMs is thought to be strongly related to the segregation of the ESCs according to the previous flow analysis. The concentrated ESCs are proposed to be located in the plug flow region according to the flow-induced ESCs segregation assumption. To identify it, the die filling experimental results are quantitatively analysed to compare with the modelling results of the established ESCs migration model and the SFR model. In addition, experimental results shown in Fig. 5 obtained by Laukli et al. [12] through the method similar to this study are also introduced to validate the modelling results. The degree of ESCs segregation increases with the increase of solid fraction, showing the same trend as the experimental results of this study.

The relative dimensions of the localized ESCs in Fig. 4(b – f) and Fig. 5 are quantitatively measured and calculated. The radius of the localized ESCs area r_{ESC} is characterised by half the mean distance between the edges of the localized ESCs area along the green lines. The relative dimensions of the localized ESCs areas in Fig. 4(b – f) are represented by r_{ESC}/R, where R is the radius of the runner, corresponding to the tube radius in Section 2. For Fig. 5(a – c), the defect bands are observed and their formation is believed to be caused by the local flow of SSMs [14,41]. This indicates no flow outside the defect bands. Therefore, the defect bands are believed to be the real walls instead of the runner walls when calculating for Fig. 5(a –c). The obtained r_{ESC}/R values are listed in Table 2.

The experimental parameters including pouring solid fraction, die cavity size (runner radius) and filling velocity (because the fill velocities are difficult to calculate due to the friction loss, the filling velocities in this research and Ref. [12] are estimated by benchmarks employing the models at $f_s = 0.33$ and $f_s = 0.30$, respectively) are introduced to the models to simulate the relative dimensions of the plug flow regions (r_c/R) using MATLAB (Mathworks, Natick, MA, USA). Fig. 6 presents the comparison between the modelling and the experimental results from both this work and Ref. [12], where good agreement is obtained. For Fig. 6(b), the pouring solid fraction is 0.28, and the experimental results located slightly above the modelling curve at $f_s = 0.3$.

The above results indicate that the relative dimensions of the localized ESCs areas yield good agreement with the plug flow region calculated by the process parameters including solid fraction, die cavity size and filling velocity. The relative dimension of the localized ESCs area can be estimated by the proposed model.

4. Discussion

The key advantage of the ESCs migration model lies in the modelling of the plug flow region caused by the yield stress of SSMs. By contrast, the widely used power law model [21] for SSMs without yield stress is introduced here to reveal the flow characteristic of the yield-pseudoplastic SSMs:
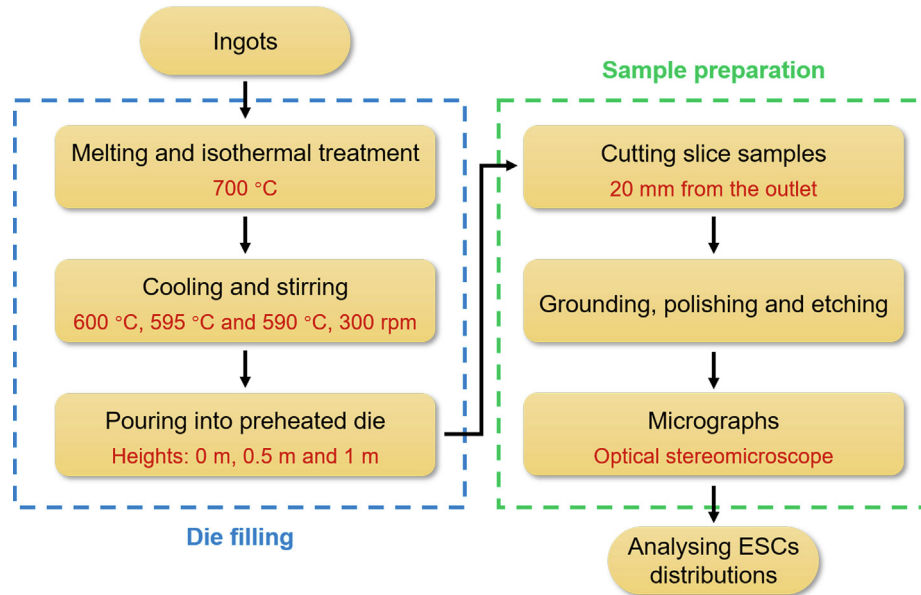
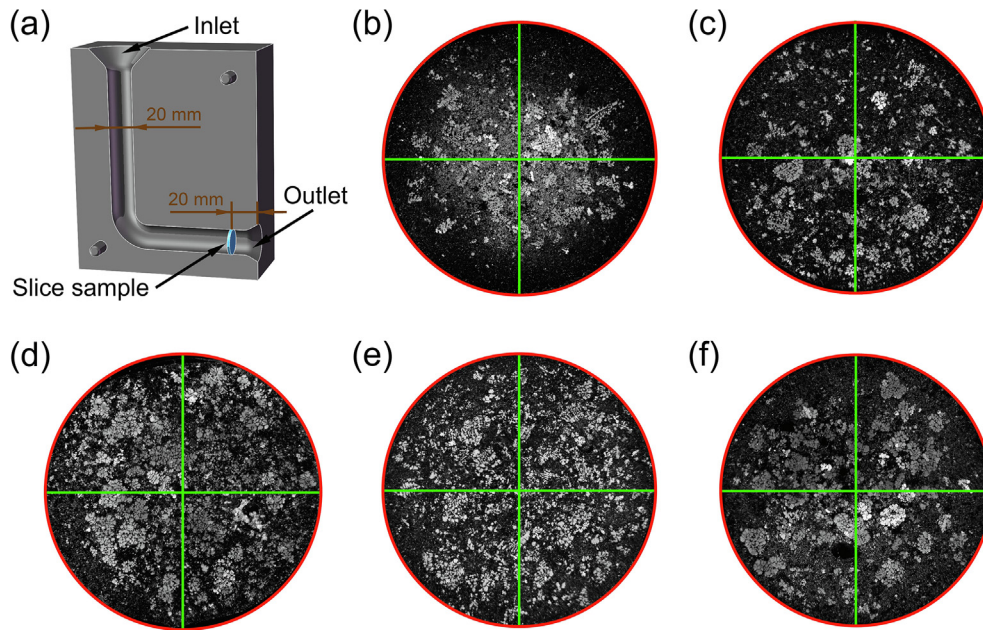**Fig. 3.** Process flow diagram of the die filling experiment.

Fig. 4. (a) Geometry of the half of the die; experimental distributions of ESCs at filling velocity of v_2 and solid fractions of (b) 0.22, (c) 0.27 and (d) 0.33; distributions of ESCs at solid fractions of 0.27 and filling velocities of (e) v_1 and (f) v_3.

$$\tau(\dot{\gamma}) = K\dot{\gamma}^n \tag{10}$$

Combining Eqs. (2), (10) and (3), the velocity profile along the radial direction ($u_{pl}(r)$) and the average flow velocity ($\bar{u}_{pl}$) of pseudoplastic SSMs are shown as Eqs. (11) and (12), respectively:

$$u_{pl}(r) = \frac{n}{n+1}\left(\frac{1}{2K}\frac{dp}{dL}\right)^{\frac{1}{n}}\left(R^{\frac{n+1}{n}} - r^{\frac{n+1}{n}}\right) \tag{11}$$

$$\bar{u}_{pl} = \frac{n}{3n+1}\left(\frac{1}{2K}\frac{dp}{dL}\right)^{\frac{1}{n}}R^{\frac{n+1}{n}} \tag{12}$$

The comparison of the relative velocity profiles ($u(r)/\bar{u}$) of the yield-pseudoplastic and pseudoplastic SSMs along the radial direction calculated by Eqs. (4), (5), (11) and (12) with different flow

exponent n is shown as Fig. 7. For pseudoplastic SSMs, the relative flow velocity is zero at $r = R$, corresponding to the maximum shear stress, and it increases with decreasing radius until reaching the maximum value at $r = 0$. In contrast, the flow velocity does not increase but keep constant after the radius decreases to a certain value (r_c) for yield-pseudoplastic SSMs. The flow exponent also influences the relative velocity profiles, where high flow exponent widens the velocity range. The effect of flow exponent seems more pronounced for pseudoplastic SSMs than yield-pseudoplastic SSMs given the presence of the plug flow region in the latter. Additionally, it is worth noting that pseudoplastic SSMs also shows a "plug flow"-like behaviour when the flow exponent is extremely low ($n < 0.1$) which is caused by the extreme shear thinning property.
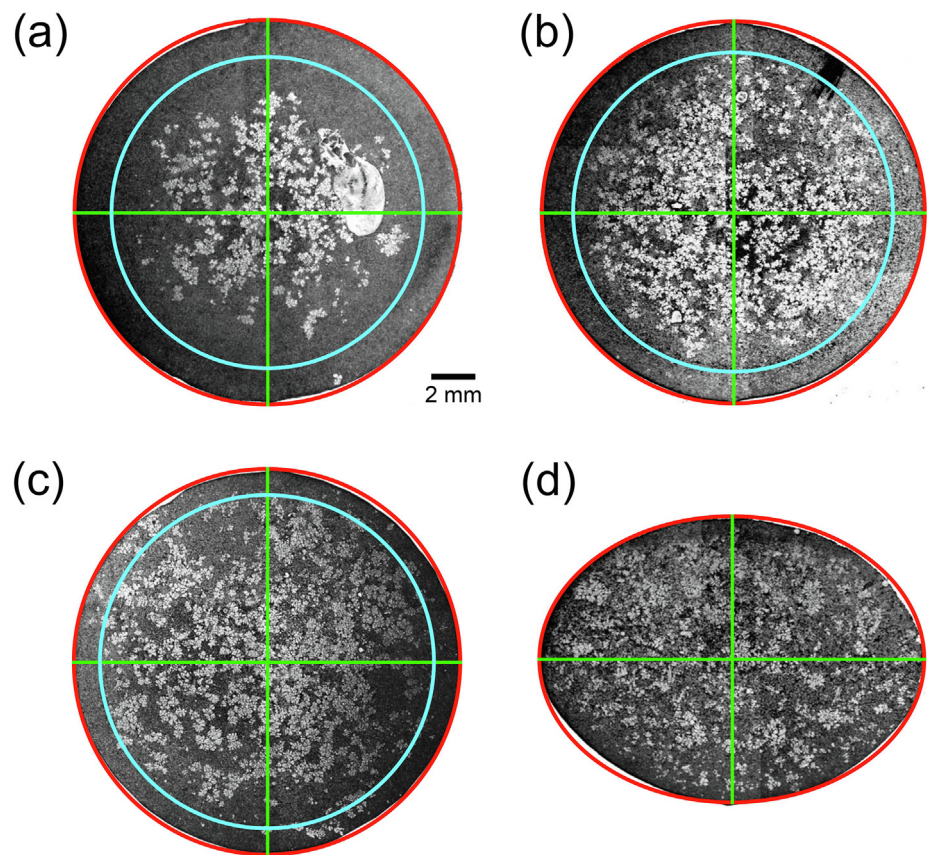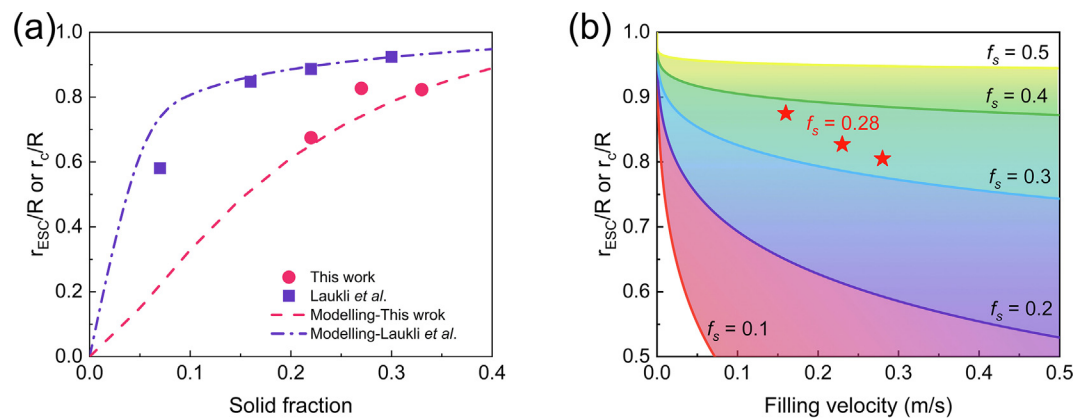
Fig. 5. Distributions of ESCs from Ref. [12] with respect to solid fraction (a) 0.07, (b) 0.16, (c) 0.22 and (d) 0.30 (with the light blue lines denoting the defect bands).

Table 2
Relative dimensions of ESCs segregation areas r_{ESC}/R.

This work				Laukli et al. [12]	
f_s	Filling velocity	r_{ESC}/R		f_s	r_{ESC}/R
0.22	v_2	0.675		0.07	0.581
0.27	v_1	0.875		0.16	0.847
	v_2	0.827		0.22	0.886
	v_3	0.805		0.30	0.924
0.33	v_2	0.823			

Fig. 6. Comparison of the relative dimensions of experimental the localized ESCs areas and modelling plug flow regions at (a) different solid fractions and (b) filling velocities (with the red stars denoting experimental results and coloured curves denoting modelling results).

The above significant differences between yield-pseudoplastic and pseudoplastic SSMs indicate that the plug flow region can be revealed only when the SSMs is treated as yield-pseudoplastic fluid. Therefore, it is reasonable to argue that the conventional con-
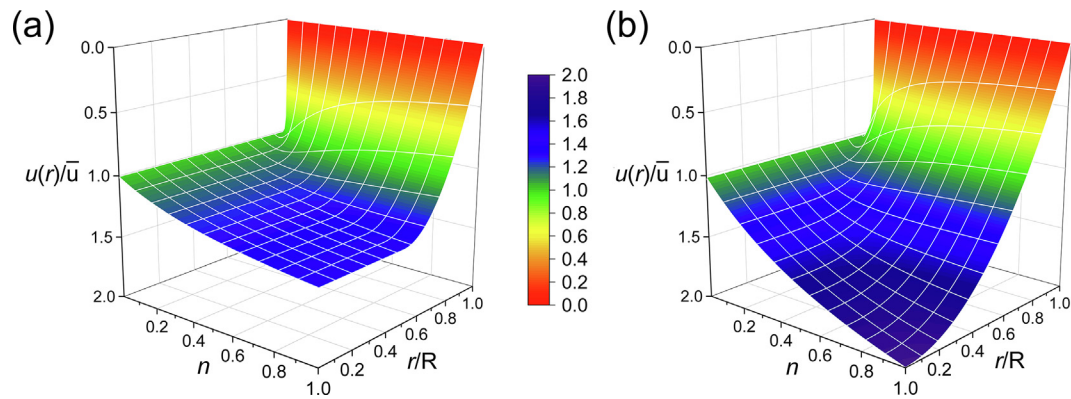
Fig. 7. 3D colour map of the relative velocity profiles of Poiseuille flow of (a) the yield-pseudoplastic SSMs with $r_c = R/2$ and (b) the pseudoplastic SSMs, indicating the effect of flow exponent on flow velocity distribution. Note that r_c may not be constant in practice due to the varying solid fraction.

cept treating the SSMs as pseudoplastic fluid limits the study of the influence of SSMs flow on such microstructural segregation.

Furthermore, the ESCs migration model is employed to simulate the filling process of semi-solid A356 alloy in a circular tube with a radius of 1 mm, and thus, analysing the influence of casting parameters on the flow-induced microstructural segregation. The simulation results are shown in Fig. 8.

According to Fig. 8(a), the ratio of the plug flow region radius to tube radius r_c/R increases with increasing of solid fraction, indicating that it is positively related to the yield stress. The ratio r_c/R is very low at a solid fraction value of 0.01; it keeps increasing to 0.95 with the solid fraction raising to 0.5; the increase rate gradually descends. The solid fraction also influences the pressure gradient significantly: the latter increases by orders of magnitude when the former increase. The evolution of pressure gradient shows that the pressure loss during the filling process of the SSM is projected to increase rapidly with increasing solid fraction at a constant filling velocity, which indicates that higher driving forces are demanded at higher solid fractions. In addition, Fig. 8(b) and (c) shows that r_c/R significantly decreases with increasing filling velocity by orders of magnitude at the same solid fraction. In other words, an enhanced filling velocity is required to maintain a relatively low r_c/R when the solid fraction of SSMs is high. A similar trend can also be observed in the simulation results in Fig. 6(b). However, the filling velocity affects not only r_c/R but the pressure gradient. A high velocity leads to a low radius of plug region as well as a high pressure gradient which cannot be neglected because the pressure generated by driving force determines whether a high level of pressure gradient in a certain length can exist (Fig. 8(c)).

Above all, the radius of the plug region is positively correlated with the solid fraction and negatively correlated with the filling velocity. Additionally, according to the filling behaviour of SSMs, reducing the plug flow region to an extremely small scale or enlarging it up to the wall may be effective to prevent the flow-induced microstructural segregation. This can be achieved by adjusting the aforementioned processing parameters. Both the solid fraction and the filling velocity are adjustable for the optimization of the segregation. The dimension of the ESCs segregation area can be reduced by choosing low solid fraction and/or high filling velocity during the process; alternatively, it can be expanded by applying high solid fraction and/or low filling velocity.

The ESCs migration model is constructed on hydrodynamics and the rheological behaviour of SSMs. Some assumptions are adopted during the modelling process in order to attain a reasonably simplified model. The SSMs are believed to be adequately stirred to an equilibrium state during the semi-solid process. Thus, the ESCs are regarded as globular or rosette-like shaped particles dis-

persed in the liquid phase of SSMs in the rheological modelling, and the translation and fragmentation of the ESCs during the filling process are neglected. The SSMs are assumed to be isothermal since the filling process is generally fast and independent of solidification. Consequently, the growth of the ESCs, the nuclear of new crystals, the solute redistribution and the natural convection related to solidification are neglected during the filling process. The rotation of the ESCs caused by the interaction between the crystals is also ignored.

Although the ESCs migration model is based on reasonable assumptions, some of the simplified factors might have minor effects on the modelling results. The morphology and size of the ESCs may vary according to different semi-solid processes which the SSMs have experienced [42–44]. The shape of the ESCs could be dendritic, rosette-like or globular. During the filling process, the crystals might also experience translation and fragmentation, if the SSMs have not been adequately stirred before filling. The shape and size changing of the ESCs can lead to variations of the rheological behaviour of SSMs, causing the change of the rheological parameters (τ_y, K and n); for example, K and n of a SSM, in which the shape of the ESCs is more complex, tend to be higher and lower, respectively [26,27,45,46]. The changes could affect the ESCs migration modelling result according to Eqs. (4) and (6). In that case, rigorous rheological tests are required for different SSMs to obtain accurate rheological parameters, which can then be used to calculate the flow-induced segregation from the model, accordingly.

The rotation of the ESCs might also affect the flow-induced segregation. The rotation could be associated with two different types of interactions: the interaction between the ESCs and liquid and the interaction amongst the ESCs. The former rotation is strongly related to the velocity profile of the liquid phase and likely to cause a fixed rotation direction of the ESCs. As illustrated in Fig. 9, the crystal is dragged by the flowing liquid to move along the flow direction during the filling process. The velocity of the liquid layer on the top of the crystal is higher than that at the bottom, which will induce the crystal to rotate clockwise. The rotation of the crystal further generates a Magnus lift force. The Magnus lift force pushes the rotating crystal towards the liquid layer of which the velocity is intensified by the rotation, i.e., upward direction in Fig. 9. This means that the rotation could lead to the ESCs migrating towards the plug flow region. Accordingly, the Magnus lift force, which is caused by the rotation resulting from interaction between the ESCs and liquid phase, is already taken into consideration by the ESCs migration model. On the other hand, the interaction among the ESCs is likely to cause crystals to rotate in random directions. The Magnus lift forces caused by different rotation
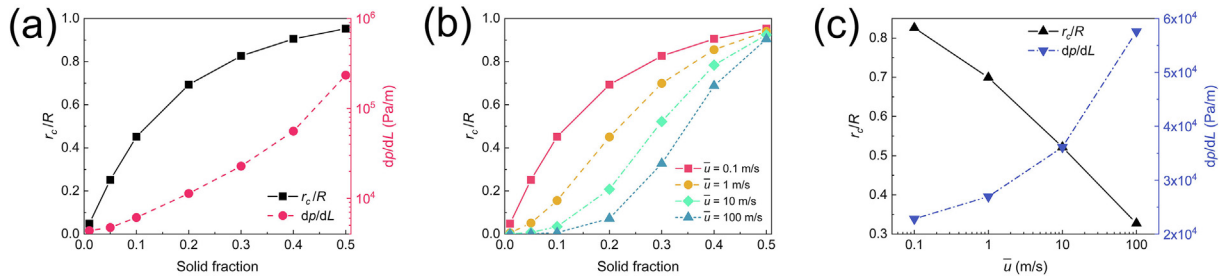
Fig. 8. Simulation results of the filling process of the semi-solid A356 alloy: (a) the ratio of plug flow region radius to tube radius (r_c/R) and axial pressure gradient ($\mathrm{d}p/\mathrm{d}L$) at different f_s under a filling velocity of 0.1 m/s, (b) r_c/R versus f_s under different filling velocities, (c) the evolutions of r_c/R and $\mathrm{d}p/\mathrm{d}L$ with filling velocity at $f_s = 0.3$.
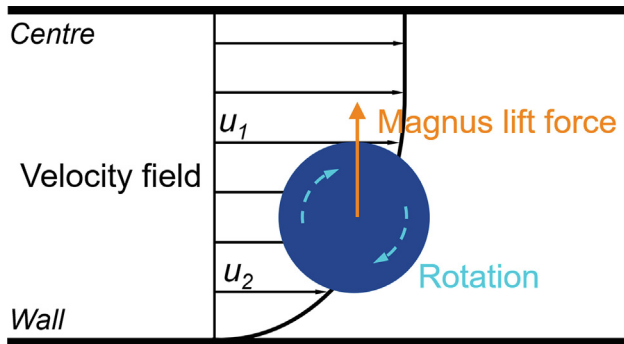
Fig. 9. Schematic diagram of the rotation and the Magnus lift force caused by the interaction between crystals and the liquid phase.

Fig. 10. Schematic diagram of the high temperature shear apparatus used for real-time in situ synchrotron X-ray radiography.

directions might push individual crystal either towards the centre or towards the wall. Therefore, it is possible that the ESCs dominated by such Magnus lift force migrate towards the wall, which might become an interference for the modelling.

5. Real-time in situ synchrotron X-ray radiography

The ESCs migration model proposed is based on the flow-induced ESCs migration mechanism underpinning the movement of the ESCs from a high shear rate layer to a low shear rate layer, in the shear flow region of the SSMs. In order to confirm and visualise the ESCs migration behaviour within the shear flow region during flow of SSMs, a real-time in situ synchrotron X-ray radiography experiment was carried on the flow process of a SSM. The real-time in situ observation offers an effective way for the visualisation of ESCs in SSMs [47].

5.1. Experimental methods

A high temperature shearing apparatus (Fig. 10) was used for the real-time synchrotron X-ray radiography experiment. Al-15Cu alloy was chosen as the experimental materials owing to its similar solidification process with A356 alloy, as well as the significant radiographic contrast between Al and Cu elements under X-rays. A plate sample cut from Al-15Cu alloy ingot was manufactured to the size of $\phi 24 \times 0.7$ mm. The sample was held between two $\phi 24 \times 1$ mm graphite parallel plates located in a furnace. The temperature of the furnace was set to 700 °C and maintained for 10 min to entirely melt the sample. Subsequently, the temperature was reduced to 615 °C with a cooling rate of ~4 °C/min to allow the sample to partially solidify into a semi-solid state. The sample was firstly sheared by rotating one of the graphite plates with a speed of 0.8 rpm for 10 min, followed by further shearing with an increased rotational speed of 4 rpm. The microstructural radiographs were recorded by the CCD camera during the whole
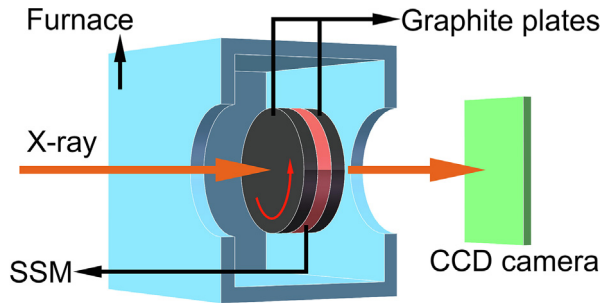
shearing process. The shearing provided decreasing shear rate along the radial direction towards the rotation centre [48].

This real-time in situ experiment was conducted at 4W1A beamline of Beijing Synchrotron Radiation Facility (BSRF). A 20 keV monochromatic beam was used, which enabled enough contrast between the ESCs and the liquid phase. The spatial resolution was 10 μm and the field of view (FOV) was 20 × 10 mm (horizon × vertical). The microstructure of the sample was recorded as 1300 × 1030 pixels images by every 1 s. The raw images were processed with the Open Source software ImageJ [49] for the analysis. A flat-field correction was applied to the raw images by subtracting the reference image before cooling. Contrast enhancement and noise reduction were applied to the images, followed by image colouring to highlight the ESCs.

5.2. Real-time in situ observation results and discussion

The real-time in situ images of ESCs during shearing at the rotation speed of 4 rpm are shown in Fig. 11. Due to size limitation, the images include just over a quarter of the sample in the FOV, but sufficiently representative for the ESCs behaviour during shearing. Under the experimental temperature, there is a number of ESCs with different sizes and morphologies in the SSM. Some of the ESCs have a rosette-like shape caused by shearing; yet some large dendrites with the size of ~2 mm still exist due to low rotation speed and short shearing time. Nevertheless, some of the small and large ESCs exhibit a migration behaviour towards the centre, which should be a consequence of the non-linear velocity profile as analysed in the previous sections. Other ESCs which do not show migration behaviour are believed to be blocked by the surrounding ESCs. The blocked ESCs may be fragmented during the shearing process [27], by which the ESCs were broken up into small ones and allowed to migrate.

Except for the non-linear velocity profile, other potential factors which may be responsible for the migration of the ESCs are discussed here. The first factor is buoyancy: the ESCs are α-Al and sus-
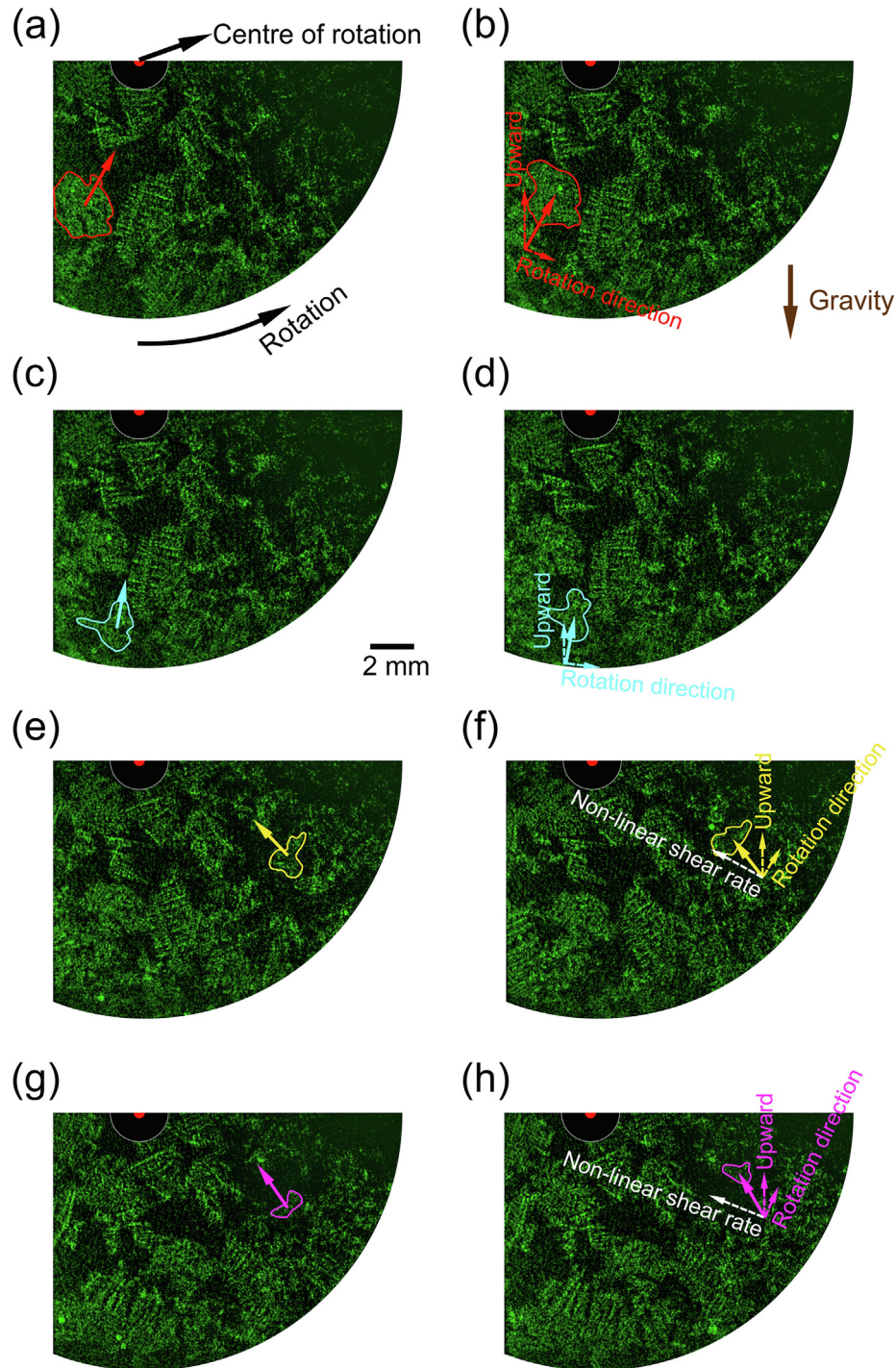
Fig. 11. Real-time in situ synchrotron X-ray radiography results: (a) 231 s, (b) 242 s, (c) 242 s, (d) 249 s, (e) 278 s, (f) 289 s, (g) 335 s and (h) 347 s after shearing under 4 rpm (with the coloured arrows denote the migrating directions of the ESCs in coloured circle lines).

pend in the Cu-enriched liquid due to the solidification process; buoyancy caused by density difference between the ESCs and the liquid could drive the ESCs upwards. The second factor is the drag force: the ESCs may be dragged along the flow direction of the liquid resulting from the drag force [50]. Taking the two factors into consideration, the migration of ESCs towards both upward and rotation directions might not be generated by non-linear velocity profile, as shown in Fig. 11(a) – (d). In fact, migrations towards the centre under the effect of non-linear velocity profile are observed in Fig. 11(e) – (h). The ESCs in the above images would

not migrate towards the illustrated direction if the driving force was composed of buoyancy and drag force. Only when the influence of non-linear shear rate is considered, can part of the buoyancy and drag force be balanced and the ESCs migrate towards the centre. This finding obtained through real-time in situ synchrotron X-ray radiography supports the flow-induce ESCs migration fundamental hypothesis of the proposed ESCs migration model.

6. Conclusions

A plug flow region without shear rate in SSMs is postulated by flow simulation employing the ESCs migration model proposed in this study. The ESCs segregation is found to be related to the plug flow region and is quantitatively predicted in this paper. The prediction of the relative dimensions of the plug flow regions agrees with the experimental relative dimensions of the localized ESCs area from both this research and the literature. Furthermore, according to the modelling results, the ESCs segregation can be controlled by adjusting the relative dimension of the plug flow region through optimizing of process parameters, such as, solid fraction, cavity size and filling velocity.

This research also presents real-time in situ X-ray synchrotron radiography results of the SSM flow under shearing in order to study the ESCs migration behaviour. The ESCs are found to migrate to the rotation centre under non-linear velocity profile. These observations reveal the nature of the ESCs migration and validate the proposed flow-induced ESCs migration mechanism.

Additionally, a semi-empirical SFR model is proposed by establishing the quantitative relationship between the rheological parameters (yield stress, flow exponent and consistency factor) and the solid fraction of SSMs. The SFR model provides a simple mathematical approach to derive the rheological parameters from solid fraction which meets the boundary conditions of $f_s = 0$ and 1. The SFR model establishes a quantitative framework for the future rheological modelling of SSMs.

Data availability

The raw/processed data required to reproduce these findings cannot be shared at this time as the data also forms part of an ongoing study.

Declaration of Competing Interest

The authors declare that they have no known competing financial interests or personal relationships that could have appeared to influence the work reported in this paper.

Acknowledgements

Appendix A. Rheological tests and data analysis

The composition of the A356 alloy is shown in Table A.1. The rheological tests were performed in controlled shear stress mode using a high-temperature rotational rheometer MCR 502 equipped with a concentric-cylinder measuring system, as described in [27]. The bob and cup were made of graphite and grooved in order to avoid the pollution and wall slip of the specimens. Cylindrical specimens with the volume of $\phi 24 \times 17$ mm cut from A356 alloy ingots were placed in the concentric-cylinder device after being polished and ultrasonically cleaned. The rheological tests proce-

dure is shown in Fig. A.1(a). The rheological experiment was performed under ten different isothermal conditions from 610 °C to 570 °C, with an interval of 10 °C. The solid fractions (f_s) corresponding to the aforementioned isothermal temperatures tested by differential scanning calorimetry (DSC) analysis using STA-449F3 were 0.01, 0.22, 0.33, 0.41, and 0.47, respectively. The alloy was pre-sheared at the shear rate of 100 s^{-1} for 60 s to ensure homogenization of the microstructure before each test. During the rheological test, the shear stress was set to linearly change from 0.1 Pa to 1000 Pa. The tests were repeated three times for each condition to ensure the reproducibility of the results.

During the rheological test, the yield behaviour of semi-solid A356 alloy was observed. The method as shown in Fig. A.1(b) is employed to identify the yield stress. It was observed that the shear rate oscillates for a low shear rate range before yielding; when the shear stress exceeds the yield stress, the shear rate stops fluctuating and begins to increase above the corresponding point ($\sim$0.1 s^{-1} in this study). The yield stresses at 570 – 610 °C (f_s = 0.01 – 0.47) in Table A.2 show a trend of non-linearly increase with decreasing temperature, as well as increasing solid fraction. The evolution of the shear stress with varying shear rate of semi-solid A356 alloy at 570 – 610 °C during the tests is illustrated in Fig. A.2. For each condition, the shear stress increases with increasing shear rate after yielding because of the fragmentation of solid particles under shear rate [51]. Moreover, the increase rate of shear stress gradually decreases with increasing shear rate, which suggest that this semi-solid alloy behaves like yield-pseudoplastic fluid. The HB model is employed to fit the experimental results. The fitting results are shown in Fig. A.2 and Table A.2. The coefficient of determination (R^2) is greater than 0.999 for each fitting curve, confirming the suitability of the HB model to reproduce the rheological behaviour of SSM.

References

[1] J. Fiocchi, A. Tuissi, C. Biffi, Heat treatment of aluminium alloys produced by laser powder bed fusion: A review, Mater. Des. 204 (2021) 109651, https://doi.org/10.1016/j.matdes.2021.109651.

[2] E. Georgantzia, M. Gkantou, G.S. Kamaris, Aluminium alloys as structural material: A review of research, Eng. Struct. 227 (2021) 111372, https://doi.org/10.1016/j.engstruct.2020.111372.

[3] T. Liu, Z. Pei, D. Barton, G.B. Thompson, L.N. Brewer, Characterization of nanostructures in a high pressure die cast Al-Si-Cu alloy, Acta Mater. 224 (2022) 117500, https://doi.org/10.1016/j.actamat.2021.117500.

[4] T.W.J. Kwok, W. Zhai, W.Y. Peh, M. Gupta, M.W. Fu, B.W. Chua, Squeeze casting for the production of metallic parts and structures, in: F.G. Caballero (Ed.), Encyclopedia of Materials: Metals and Alloys, Elsevier, Oxford, 2022, pp. 87–99, https://doi.org/10.1016/B978-0-12-819726-4.00038-7.

[5] L. Stemper, B. Mitas, T. Kremmer, S. Otterbach, P.J. Uggowitzer, S. Pogatscher, Age-hardening of high pressure die casting AlMg alloys with Zn and combined Zn and Cu additions, Mater. Des. 181 (2019) 107927, https://doi.org/10.1016/j.matdes.2019.107927.

[6] X. Hu, Q. Zhu, S. Midson, H. Atkinson, H. Dong, F. Zhang, Y. Kang, Blistering in semi-solid die casting of aluminium alloys and its avoidance, Acta Mater. 124 (2017) 446–455, https://doi.org/10.1016/j.actamat.2016.11.032.

[7] S. Tzamtzis, H. Zhang, N.H. Babu, Z. Fan, Microstructural refinement of AZ91D die-cast alloy by intensive shearing, Mater. Sci. Eng. A 527 (12) (2010) 2929–2934, https://doi.org/10.1016/j.msea.2010.01.013.

[8] X. Jiao, C. Liu, J. Wang, Z. Guo, J. Wang, Z. Wang, J. Gao, S. Xiong, On the characterization of microstructure and fracture in a high-pressure die-casting Al-10 wt% Si alloy, Prog. Nat. Sci.: Mater. Int. 30 (2) (2020) 221–228, https://doi.org/10.1016/j.pnsc.2019.04.008.

[9] E. Lordan, Y. Zhang, K. Dou, A. Jacot, C. Tzileroglou, P. Blake, Z. Fan, On the probabilistic nature of high-pressure die casting, Mater. Sci. Eng., A 817 (2021) 141391, https://doi.org/10.1016/j.msea.2021.141391.

[10] H. Laukli, O. Lohne, S. Sannes, H. Gjestland, L. Arnberg, Grain size distribution in a complex AM60 magnesium alloy die casting, Int. J. Cast Met. Res. 16 (6) (2003) 515–521, https://doi.org/10.1080/13640461.2003.11819629.

[11] Y. Zhou, Z. Guo, S.-M. Xiong, Effect of runner design on the externally solidified crystals in vacuum die-cast Mg-3.0 Nd-0.3 Zn-0.6 Zr alloy, J. Mater. Process. Technol. 267 (2019) 366–375, https://doi.org/10.1016/j.jmatprotec.2018.12.032.

[12] H. Laukli, C. Gourlay, A. Dahle, Migration of crystals during the filling of semi-solid castings, Metall. Mater. Trans. A 36 (3) (2005) 805–818, https://doi.org/10.1007/s11661-005-1011-5.

Table A.1

A356 alloy composition.

Element	Si	Mg	Fe	Cu	Ti	Sr	Zn	Ni	Al
Wt. %	7.128	0.346	0.111	0.089	0.145	0.0144	0.006	0.005	Balance
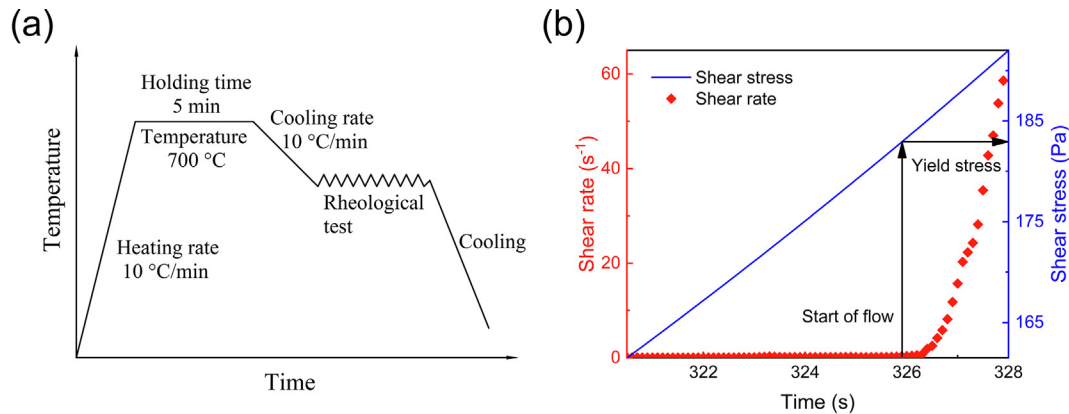
Fig. A.1. (a) Rheological experimental procedure; (b) method to identify the yield stress of semi-solid A356 alloy at 590 °C.

Table A.2

Yield stress and fitting parameters of the HB modelling results.

Temperature (°C)			570	580	590	600	610
Solid fraction f_s			0.47	0.41	0.33	0.22	0.01
Yield stress τ_y (Pa)		Avg.	601.02	363.24	180.30	12.25	6.05
		Std.	24.98	4.25	10.69	0.43	0.17
Fitting parameters	n	Avg.	0.16	0.25	0.37	0.54	0.84
		Std.	0.01	0.02	0.03	0.06	0.07
	K	Avg.	14.77	7.15	2.07	0.15	0.17
		Std.	3.98	2.76	0.21	0.04	0.03
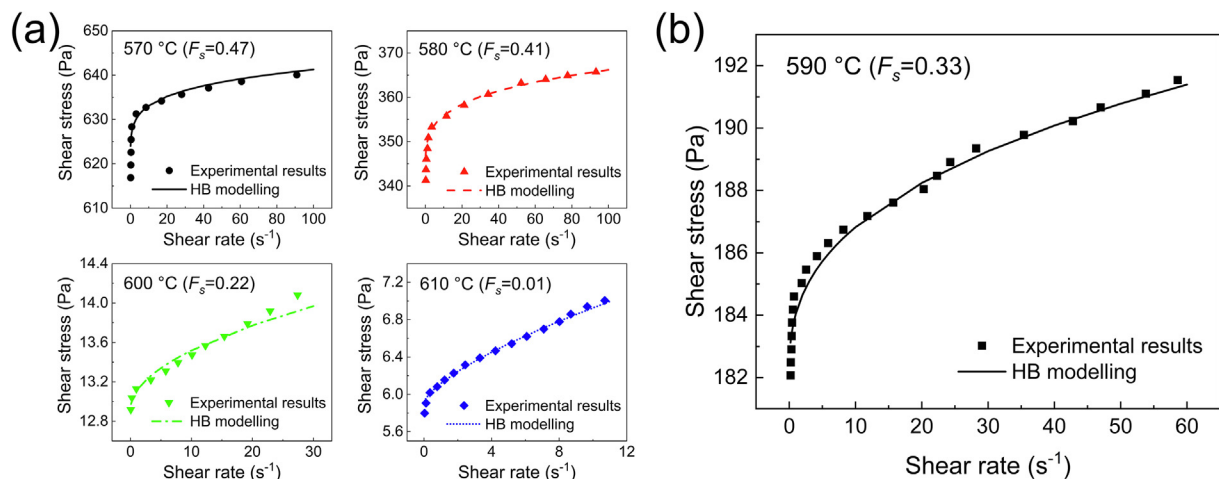
Fig. A.2. Flow curves of experimental and HB modelling results at (a) 570 °C ($f_s = 0.47$), 580 °C ($f_s = 0.41$), 600 °C ($f_s = 0.22$) and 610 °C ($f_s = 0.01$) and (b) 590 °C ($f_s = 0.33$).

[13] X. Li, S. Xiong, Z. Guo, On the tensile failure induced by defect band in high pressure die casting of AM60B magnesium alloy, Mater. Sci. Eng., A 674 (2016) 687–695, https://doi.org/10.1016/j.msea.2016.08.039.

[14] C.M. Gourlay, A.K. Dahle, H.I. Laukli, Segregation band formation in Al-Si die castings, Metall. Mater. Trans. A 35 (9) (2004) 2881–2891, https://doi.org/10.1016/j.msea.2016.08.039.

[15] B. Wang, S. Xiong, Effects of shot speed and biscuit thickness on externally solidified crystals of high-pressure diet cast AM60B magnesium alloy, Trans. Nonferrous Met. Soc. China 21 (4) (2011) 767–772, https://doi.org/10.1016/S1003-6326(11)60778-4.

[16] C. Bi, S. Xiong, X. Li, Z. Guo, Development of a fluid-particle model in simulating the motion of external solidified crystals and the evolution of

defect bands in high-pressure die casting, Metall. Mater. Trans. B 47 (2) (2016) 939–947, https://doi.org/10.1007/s11663-016-0591-3.

[17] M. Wu, X. Li, Z. Guo, S. Xiong, Effects of process parameters on morphology and distribution of externally solidified crystals in microstructure of magnesium alloy die castings, China Foundry 15 (2) (2018) 139–144, https://doi.org/10.1007/s41230-018-7242-z.

[18] A. Dahle, D. StJohn, Rheological behaviour of the mushy zone and its effect on the formation of casting defects during solidification, Acta Mater. 47 (1) (1998) 31–41, https://doi.org/10.1016/S1359-6454(98)00342-5.

[19] K. Wang, H. Jiang, Q. Wang, B. Ye, W. Ding, A novel method to achieve grain refinement in aluminum, Metall. Mater. Trans. A 47 (10) (2016) 4788–4794, https://doi.org/10.1007/s11661-016-3668-3.

[20] E. Giraud, M. Suery, M. Coret, High temperature compression behavior of the solid phase resulting from drained compression of a semi-solid 6061 alloy, Mater. Sci. Eng., A 532 (2012) 37–43, https://doi.org/10.1016/j.msea.2011.10.059.

[21] M.C. Flemings, Behavior of metal alloys in the semisolid state, Metall. Trans. A 22 (5) (1991) 957–981, https://doi.org/10.1007/BF02661090.

[22] M. Braccini, C. Martin, A. Tourabi, Y. Bréchet, M. Suery, Low shear rate behavior at high solid fractions of partially solidified Al–8 wt.% Cu alloys, Mater. Sci. Eng. A 337 (1–2) (2002) 1–11, https://doi.org/10.1016/S0921-5093(02)00042-4.

[23] D. Brabazon, D. Browne, A. Carr, Experimental investigation of the transient and steady state rheological behaviour of Al–Si alloys in the mushy state, Mater. Sci. Eng. A 356 (1–2) (2003) 69–80, https://doi.org/10.1016/S0921-5093(03)00158-8.

[24] H.V. Atkinson, Modelling the semisolid processing of metallic alloys, Prog. Mater. Sci. 50 (3) (2005) 341–412, https://doi.org/10.1016/j.pmatsci.2004.04.003.

[25] M. Paes, E. Zoqui, Semi-solid behavior of new Al–Si–Mg alloys for thixoforming, Mater. Sci. Eng. A 406 (1–2) (2005) 63–73, https://doi.org/10.1016/j.msea.2005.07.018.

[26] X. Hu, Q. Zhu, H. Atkinson, H. Lu, F. Zhang, H. Dong, Y. Kang, A time-dependent power law viscosity model and its application in modelling semi-solid die casting of 319s alloy, Acta Mater. 124 (2017) 410–420, https://doi.org/10.1016/j.actamat.2016.11.031.

[27] Z. Ma, H. Zhang, X. Zhang, X. Wu, H. Fu, L. Jia, H. Zhang, Rheological behaviour of partially solidified A356 alloy: Experimental study and constitutive modelling, J. Alloys Compd. 803 (2019) 1141–1154, https://doi.org/10.1016/j.jallcom.2019.06.345.

[28] P. Seo, C. Kang, Process analysis of semi-solid die casting by viscosity measurement of rheological materials and their experimental evaluation, in: Proceedings of the 7th International Conference on Semi-Solid Processing of Alloys and Composites. Tsukuba: National Institute of Advanced Industrial Science and Technology, Japan Society for Technology of Plasticity, 2002, pp. 515–520.

[29] M. Modigell, A. Pola, M. Tocci, Rheological characterization of semi-solid metals: A review, Metals 8 (4) (2018) 245, https://doi.org/10.3390/met8040245.

[30] W. Herschel, R. Bulkley, Measurement of consistency as applied to rubber-benzene solutions, Am. Soc. Test Mater. 26 (2) (1926) 621–633.

[31] H. Liu, Pipeline Engineering, first ed., CRC Press, Boca Raton, 2003.

[32] Z. Ma, H. Zhang, H. Fu, Y. Yang, J. Wang, M. Du, H. Zhang, Insights into the rheological modeling of semi-solid metals: Theoretical and simulation study, J. Mater. Sci. Technol. 100 (2022) 182–192, https://doi.org/10.1016/j.jmst.2021.05.041.

[33] V. Laxmanan, M. Flemings, Deformation of semi-solid Sn-15 pct Pb alloy, Metall. Trans. A 11 (12) (1980) 1927–1937, https://doi.org/10.1007/BF02655112.

[34] C. Quaak, Rheology of partial solidified aluminium composites, Ph.D. thesis, Ph. D. Thesis, TU Delft, 1996.

[35] B.R. Munson, T.H. Okiishi, W.W. Huebsch, A.P. Rothmayer, Fundamentals of Fluid Mechanics, sixth ed., John Wiley & Sons, Hoboken, 2009.

[36] S.H. Maron, P.E. Pierce, Application of ree-eyring generalized flow theory to suspensions of spherical particles, J. Colloid Sci. 11 (1) (1956) 80–95, https://doi.org/10.1016/0095-8522(56)90023-X.

[37] S. Mueller, E. Llewellin, H. Mader, The rheology of suspensions of solid particles, Proc. R. Soc. A 466 (2116) (2010) 1201–1228, https://doi.org/10.1098/rspa.2009.0445.

[38] L. Heymann, S. Peukert, N. Aksel, On the solid-liquid transition of concentrated suspensions in transient shear flow, Rheol. Acta 41 (4) (2002) 307–315, https://doi.org/10.1007/s00397-002-0227-1.

[39] Z. Ma, H. Zhang, W. Song, X. Wu, L. Jia, H. Zhang, Pressure-driven mold filling model of aluminum alloy melt/semi-solid slurry based on rheological behavior, J. Mater. Sci. Technol. 39 (2020) 14–21, https://doi.org/10.1016/j.jmst.2019.07.048.

[40] T. Iida, R.I. Guthrie, The Physical Properties of Liquid Metals, first ed., Clarendon Press, Oxford, 1988.

[41] C. Gourlay, A. Dahle, Dilatant shear bands in solidifying metals, Nature 445 (7123) (2007) 70, https://doi.org/10.1038/nature05426.

[42] Z. Chang, N. Su, Y. Wu, Q. Lan, L. Peng, W. Ding, Semisolid rheoforming of magnesium alloys: A review, Mater. Des. 195 (2020) 108990, https://doi.org/10.1016/j.matdes.2020.108990.

[43] Y. Chen, L. Zhang, W. Liu, G. Wu, W. Ding, Preparation of Mg-Nd-Zn-(Zr) alloys semisolid slurry by electromagnetic stirring, Mater. Des. 95 (2016) 398–409, https://doi.org/10.1016/j.matdes.2016.01.131.

[44] S. Terzi, L. Salvo, M. Suery, A. Dahle, E. Boller, In situ microtomography investigation of microstructural evolution in Al-Cu alloys during holding in semi-solid state, Trans. Nonferrous Met. Soc. China 20 (2010) s734–s738, https://doi.org/10.1016/S1003-6326(10)60572-9.

[45] J. Yurko, M. Flemings, Rheology and microstructure of semi-solid aluminum alloys compressed in the drop-forge viscometer, Metall. Mater. Trans. A 33 (8) (2002) 2737–2746, https://doi.org/10.1007/s11661-002-0396-7.

[46] T. Liu, H. Atkinson, P. Kapranos, D. Kirkwood, S. Hogg, Rapid compression of aluminum alloys and its relationship to thixoformability, Metall. Mater. Trans. A 34 (7) (2003) 1545–1554, https://doi.org/10.1007/s11661-003-0266-y.

[47] J. Fonseca, C. O'Sullivan, T. Nagira, H. Yasuda, C. Gourlay, In situ study of granular micromechanics in semi-solid carbon steels, Acta Mater. 61 (11) (2013) 4169–4179, https://doi.org/10.1016/j.actamat.2013.03.043.

[48] T.G. Mezger, The Rheology Handbook: for Users of Rotational and Oscillatory Rheometers, fourth ed., Vincentz Network GmbH & Co KG, Hanover, 2014.

[49] C.A. Schneider, W.S. Rasband, K.W. Eliceiri, NIH Image to ImageJ: 25 years of image analysis, Nat. Methods 9 (7) (2012) 671–675, https://doi.org/10.1038/nmeth.2089.

[50] G. Falkovich, Fluid Mechanics: A Short Course for Physicists, Cambridge University Press, Cambridge, 2011.

[51] P. Das, S.K. Samanta, P. Dutta, Rheological behavior of Al-7Si-0.3Mg alloy at mushy state, Metall. Mater. Trans. B 46 (3) (2015) 1302–1313, https://doi.org/10.1007/s11663-015-0290-5.